

Computing the committor with the committor to study the transition state ensemble

Received: 12 January 2024

Accepted: 14 May 2024

Published online: 05 June 2024

 Check for updatesPeilin Kang ¹, Enrico Trizio ^{1,2} & Michele Parrinello ¹ 

The study of the kinetic bottlenecks that hinder the rare transitions between long-lived metastable states is a major challenge in atomistic simulations. Here we propose a method to explore the transition state ensemble, which is the distribution of configurations that the system passes through as it translocates from one metastable basin to another. We base our method on the committor function and the variational principle that it obeys. We find its minimum through a self-consistent procedure that starts from information limited to the initial and final states. Right from the start, our procedure allows the sampling of very many transition state configurations. With the help of the variational principle, we perform a detailed analysis of the transition state ensemble, ranking quantitatively the degrees of freedom mostly involved in the transition and enabling a systematic approach for the interpretation of simulation results and the construction of efficient physics-informed collective variables.

Many important physicochemical transformations such as crystallization, chemical reactions and protein folding take place on a time scale that is not directly accessible to microscopic simulations. These processes are referred to as rare events and are hindered by kinetic bottlenecks that slow the rate of transition between metastable states. Such kinetic bottlenecks are present whenever the metastable states are separated by a high free-energy set of configurations that we refer to as the transition state ensemble (TSE). Finding and analyzing this region is of the utmost theoretical and practical importance. For example, identifying the transition state is considered the holy grail when it comes to chemical reactions¹, as it provides precious information about reaction mechanisms and rates², or when dealing with proteins, as it can provide insight into their dynamics^{3–5}.

In the vast rare event literature^{6–11}, the determination of the TSE is usually the culmination of the simulation. In this Article, instead, we make the determination of the TSE the first and key aspect of our investigation. The theoretical tool that allows this change of perspective is the committor function $q(\mathbf{x})$, introduced by Kolmogorov¹². Given two metastable states, A and B, $q(\mathbf{x})$ gives the probability that, starting from configuration \mathbf{x} , the system ends in B without having

first passed by A, and as a consequence, it is conventionally used to identify the TSE as the set of configurations for which $q(\mathbf{x}) \simeq \frac{1}{2}$ (refs. 13–24). Once $q(\mathbf{x})$ is known, properties such as the transition rate between A and B, the density of reactive trajectories or the reactive fluxes can be computed^{17,19,20}. Unfortunately, the determination of $q(\mathbf{x})$ is challenging, and in the transition path sampling literature^{18,22,25}, it has been mostly estimated for curated sets of points via committor analysis. However, such an approach can be computationally expensive and often dependent on the choice of the criteria used to determine whether a given trajectory is committed to either basin A or B (ref. 26).

An alternative to such an approach is based on the theory of Kolmogorov^{20,27–29}, who showed that $q(\mathbf{x})$ can be determined as the solution of a partial differential equation²⁰ that obeys the boundary conditions $q(\mathbf{x}_A) = 0$ and $q(\mathbf{x}_B) = 1$, where \mathbf{x}_A and \mathbf{x}_B denote two configurations belonging to basin A and B, respectively. Unfortunately, solving such a multidimensional equation for real systems poses insurmountable problems. However, under the hypothesis of overdamped dynamics, the solution of the Kolmogorov equation can also be obtained by following a variational approach that amounts to minimizing a functional

¹Atomistic Simulations, Italian Institute of Technology, Genova, Italy. ²Department of Materials Science, Università di Milano-Bicocca, Milano, Italy.

✉ e-mail: michele.parrinello@iit.it

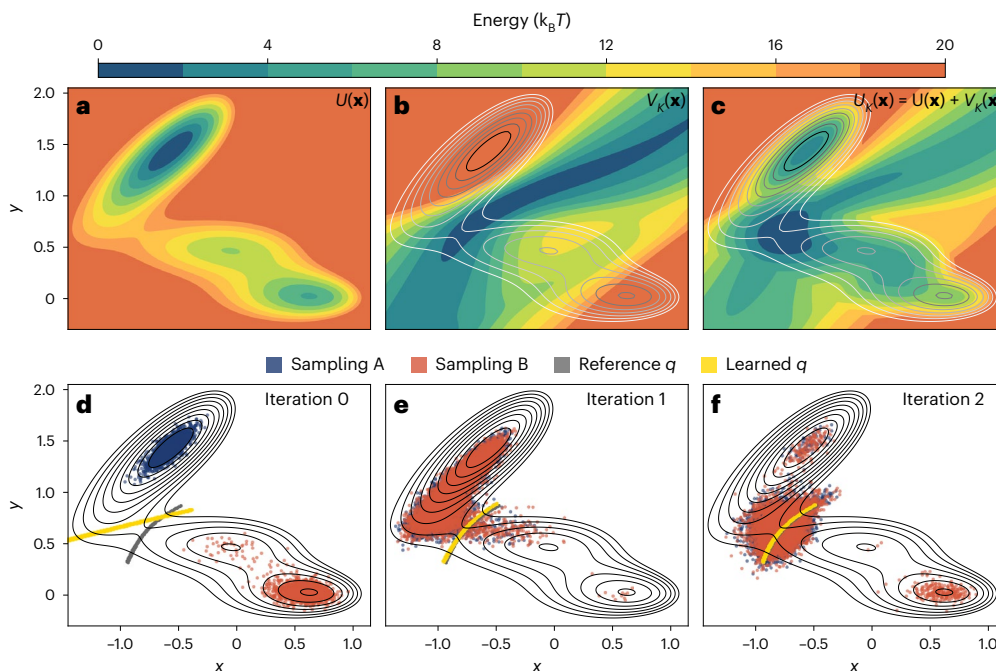


Fig. 1 | Müller-Brown potential. We illustrate how our iterative procedure proceeds when applied to the computation of the committor function of the Müller-Brown potential. **a–c**, The contour plots of the potential $U(\mathbf{x})$ (**a**), the bias $V_K(\mathbf{x})$ (**b**) and the effective biased potential $U_K(\mathbf{x}) = V_K(\mathbf{x}) + U(\mathbf{x})$ (**c**). Here, the committor is computed from numerical integration. **d–f**, Scatter plots reporting the results of the sampling cycles through the iterations needed to converge the committor using our procedure. The corresponding iteration number is given by

the top-right labels. Points sampled starting from basin A are depicted in blue, whereas those from B are in red. For each iteration, the -0.5 value of the learned committor function at that iteration (yellow line) is compared with the reference value from numerical integration (gray line) for the physically relevant part of the transition state region. In the lower panels, the original potential energy surface is represented by isolines.

of the committor $\mathcal{K}[q(\mathbf{x})]$, which, neglecting immaterial multiplicative constants, can be written as

$$\mathcal{K}[q(\mathbf{x})] = \langle |\nabla q(\mathbf{x})|^2 \rangle_{U(\mathbf{x})}, \quad (1)$$

where, in the differential operator, the derivatives pertinent to the i th atom of mass m_i are performed with respect to its mass-weighted Cartesian coordinates $\sqrt{m_i} \mathbf{x}_i$, the average is over the Boltzmann ensemble driven by the interaction potential $U(\mathbf{x})$ at the inverse temperature β and the boundary conditions $q(\mathbf{x}_A) = 0$ and $q(\mathbf{x}_B) = 1$ are implied. Moreover, the reaction rate v_R is proportional to the minimum of the functional \mathcal{K}_m . For further discussion on equation (1) and its extension to the general Langevin dynamics, see ‘Motivation of variational principle’ section in Methods and the excellent review by W. E. and E. Vanden-Eijnden²⁰.

Unfortunately, even when using the variational approach, evaluating $q(\mathbf{x})$ remains challenging. To understand this sampling difficulty, we notice that, when dealing with rare events, trajectories started in A have a very small probability of ending in B; thus, $q(\mathbf{x}) \approx 0$ for $\mathbf{x} \in A$, and similarly, when a trajectory is started in B, it will most probably remain in B; thus, $q(\mathbf{x}) \approx 1$ for $\mathbf{x} \in B$. As a consequence, $|\nabla q(\mathbf{x})|^2$ is substantially different from zero only in those regions in which $q(\mathbf{x})$ goes from 0 to 1 as it passes through the transition state region, where it is at its largest. This is hardly surprising since the probability of going from A to B, which $q(\mathbf{x})$ reflects, is crucially determined by the TSE, the very set of configurations that are difficult to sample in a rare event scenario.

This difficulty has been recognized, and different remedies have been proposed. In ref. 27, it is shown that a uniform sampling can be done in small systems, but it is not, in general, a viable strategy. For this reason, a variety of enhanced sampling methods have been suggested to collect configurations that pertain to the TSE so as to estimate accurately $\mathcal{K}[q(\mathbf{x})]$ and eventually minimize it. The methods used range from metadynamics²⁸ to a combination of umbrella sampling and

parallel tempering²³. If the objective is to compute $q(\mathbf{x})$, this approach is wasteful since the TSE is a small portion of configuration space, and even if one uses enhanced sampling methods, it is rarely visited. Furthermore, the calculation of the committor comes at the end of what amounts to having solved the rare event problem, and since these methods are dependent on the choice of the collective variable (CV), the accuracy of the result is, at times, difficult to assess.

Methods that are similar in spirit to ours are described in ref. 30, where short nonequilibrium trajectories are harvested iteratively closer to the TS, and in refs. 22, 24, 26, which are based on path sampling and, thus, like ours, are focused from the start on sampling the region close to the TSE. However, these methods are somewhat complex and can only be applied if the path sampling approach is at least in part successful. Thus, similarly to the other approaches described above, all these methods require that the rare event problem is at least partially already solved, a limitation also shared by the method presented in ref. 31, which allows computing the $q(\mathbf{x})$ from long equilibrium trajectories.

Instead, our approach relies only on the knowledge of the initial and final state and can be initiated just by performing unbiased simulations in the initial and final metastable basins. To sample the TSE, we use to our advantage what appears to be a handicap. To this effect, we introduce the following committor-dependent bias potential:

$$V_K(\mathbf{x}) = -\frac{1}{\beta} \log(|\nabla q(\mathbf{x})|^2). \quad (2)$$

It follows from the general behavior of $q(\mathbf{x})$ that such a bias is repulsive in A and B, where $\nabla q(\mathbf{x}) \approx 0$, and becomes highly attractive close to the TSE, where $q(\mathbf{x})$ rises very rapidly from 0 to 1. In particular, the maximum value is reached for $q(\mathbf{x}) \approx \frac{1}{2}$ (Fig. 1b and Supplementary Fig. 2), and, as a consequence, such a bias has the appealing property of driving the sampling toward the region that is conventionally associated with the TSE. In addition, we notice that the standard TSE definition

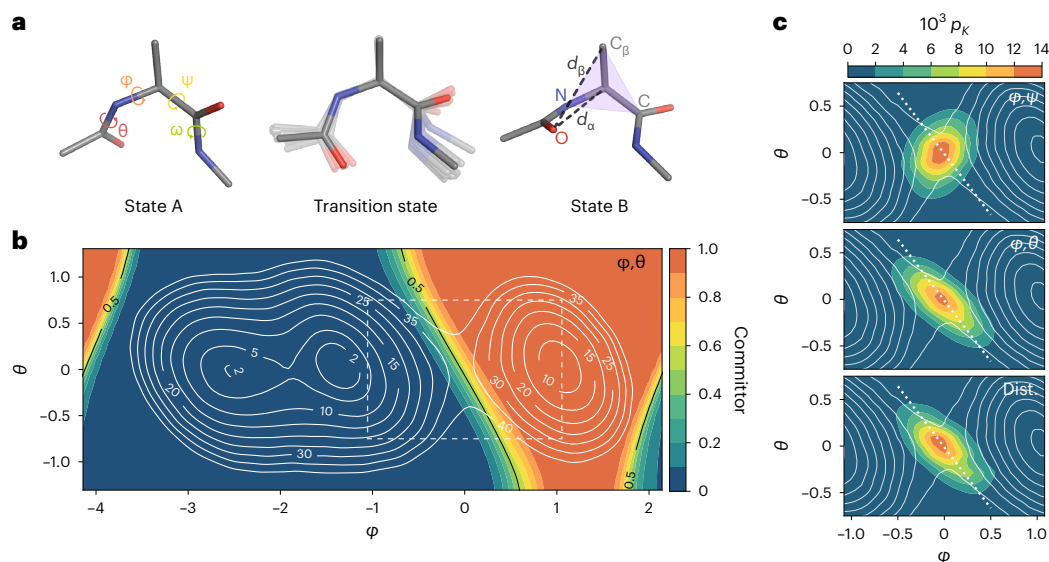


Fig. 2 | Alanine dipeptide. **a**, Snapshots of alanine dipeptide conformations in metastable and transition states. The relevant torsional angles of the peptide are depicted for state A, whereas the most relevant distances and the plane defined by the N, C_β, C atoms are illustrated for state B. For the transition state, we report in transparency a superimposition of 20 configurations from the TSE and, in solid color, the medoid of such an ensemble. Carbon atoms are depicted in gray, oxygen in red and nitrogen in blue, whereas hydrogens are omitted for clarity. **b**, Projection of alanine free energy surface (white isolines) and of the learned

committor value $q(\phi, \theta)$ (colormap) in the ϕ, θ plane. **c**, Contour plot the Kolmogorov distribution p_K on the transition region, highlighted in **b** by a dotted white box, according to committor-based bias potentials trained on different descriptors sets ϕ, ψ angles, ϕ, θ angles and a set of distances (Dist.), as indicated by the top-right labels. The white isolines depict the underlying free energy surface, and the dashed white line reports the linear relation between ϕ, θ for the TSE configurations proposed in ref. 35.

can be enriched by explicitly taking into account also the probability that the configuration \mathbf{x} is actually visited, which is only implicitly considered in the standard approach. Indeed, in that case, the points selected for computing the committor are generated in a transition path sampling run or even along actual reactive trajectories.

Such considerations motivate us to define the TSE ensemble by what we call the Kolmogorov distribution

$$p_K(\mathbf{x}) = \frac{e^{-\beta U_K(\mathbf{x})}}{Z_K} \text{ with } U_K(\mathbf{x}) = U(\mathbf{x}) + V_K(\mathbf{x}), \quad (3)$$

where U_K is the biased potential and $Z_K = \int d\mathbf{x} e^{-\beta U_K(\mathbf{x})}$ is the corresponding partition function. Somehow reassuringly, $p_K(\mathbf{x})$ is also closely related to the Kolmogorov functional since $\mathcal{K}[q(\mathbf{x})] = \frac{Z_K}{Z_B}$, thus allowing it to be rewritten as

$$\mathcal{K}[q(\mathbf{x})] = \left\langle \frac{1}{|\nabla q(\mathbf{x})|^2} \right\rangle_{U_K}^{-1}. \quad (4)$$

While equivalent to equation (1), this expression suggests that it would be more profitable to use U_K to generate the points needed to estimate statistically $\mathcal{K}[q(\mathbf{x})]$, since this approach automatically enhances a physically meaningful TSE sampling (Fig. 1c).

However, at first sight, this may still appear to be a chicken-and-egg problem since, to get the committor, one needs good sampling, and in turn, to get good sampling, one needs the committor. We show here that this dilemma can be resolved by setting up a self-consistent iterative procedure, described in Methods. This procedure starts from an initial estimate of the committor. Such an estimate needs to have the property of being 0 for $\mathbf{x} \in A$ and 1 for $\mathbf{x} \in B$ and of interpolating smoothly between the two basins. One simple way of obtaining an initial guess is to express it as a classifier trained using data obtained by performing unbiased simulations in the two basins.

After convergence is reached, a large number of TSE configurations can be harvested and the property of the TSE analyzed in great

and illuminating detail. This analysis is facilitated by the fact that we express $q(\mathbf{x})$ as a neural network^{27–29,32} (NN) $q_\theta(d(\mathbf{x}))$ whose weights are denoted by θ and whose input features $d(\mathbf{x})$ are a set of physical descriptors that simplify the imposition of the problem symmetries, decrease the noise and help in understanding the physics of the problem. In particular, we shall use the approach from ref. 33 to rank the relevance of the descriptors.

The variational principle also provides a powerful way of choosing the descriptors. In fact, the inclusion of physically relevant descriptors lowers the variational bound, while adding physically irrelevant descriptors has very little effect. Moreover, in complex systems and at finite temperatures, the TSE is not associated with only one structure and its quasi-harmonic excited vibrational states. Rather, it is populated by different competing structures. To sort them out, we use the k -medoids clustering method³⁴, which also associates to each cluster a medoid configuration that best represents the cluster structure. The combination of these tools greatly facilitates the physical interpretation of the results and guides the researcher's attention to the degrees of freedom that matter the most. It is to reflect the ability of our method to analyze the TSE in excruciating detail that we have chosen the manuscript title.

We first test our method on the numerically solvable example of the Müller potential and proceed then to discuss the classical example of alanine dipeptide in a vacuum, a complex chemical reaction and the folding of a small protein. In all the last three examples, our analysis leads to physically meaningful insight, even on a much-studied problem like that of alanine dipeptide. The details of the numerical implementation are discussed in 'Self-consistent iterative procedure', 'Optimization strategy' and 'Sampling the Kolmogorov ensemble' sections in Methods.

Results

Müller–Brown potential

The first application of our methods is to the two-dimensional Müller–Brown potential, which is often used to test new methods since,

in this case, the committor can be numerically evaluated (Supplementary Section 2b).

In the bottom panels of Fig. 1, we show the evolution of the segment of the isocommittor line $q(\mathbf{x}) = \frac{1}{2}$ that overlaps the TSE and compare it with the result coming from numerical integration. In the first iteration, in which the only data available are those coming from the metastable states, the first guess for $q(\mathbf{x})$ is nothing but a classifier. Thus, at this first stage, the isocommittor line is just a straight line that divides the two metastable basins. However, as more and more TSE data are collected under the action of the bias $V_{\mathcal{K}}(\mathbf{x})$, the isocommittor converges to its correct value after only a few iterations, and an accurate description of the whole $p_{\mathcal{K}}(\mathbf{x})$ is obtained after only a few more iterations (Supplementary Fig. 8). Moreover, it can be seen that, as the iterative process progresses, the TSE is better and better sampled.

Alanine dipeptide

As a second and more physically relevant example, we study the transition of alanine dipeptide in a vacuum between the C_{7eq} (A) and C_{7ax} (B) conformers, which is one of the most studied rare event models. Its conformational landscape is spanned by the four dihedral angles φ , θ , ψ and ω that measure the orientation of the two peptides relative to the more rigid tetrahedron formed by the N, C, C_{α} and C_{β} atoms (Fig. 2a). The dihedral angles φ and ψ have been found to be good CVs when used in enhanced sampling methods³³. It has also been found in transition path sampling studies³⁵ that, in the configurations that belong to the TSE, the angles φ and θ are, modulus a constant, approximately linearly anti-correlated (that is, $\theta \approx -\varphi$). To demonstrate the ability of our method to recover these results, we first use φ , θ , ψ and ω as descriptors. However, rather than using all of them at once, we start with one, and then we systematically add all the others.

The rationale for this procedure is that, given the variational property of the functional $\mathcal{K}[q(\mathbf{x})]$, an indication of the relevance of an added dihedral angle will be its ability to lower the minimum value \mathcal{K}_m .

The number of calculations to be performed is reduced if we first note that, to satisfy the boundary conditions, φ has to be part of the descriptor set. Thus, we compute \mathcal{K}_m first using only φ and then study all possible combinations of φ with the remaining torsional angles. The results of these calculations are illustrated in Supplementary Table 2, where it can be seen that including θ in the descriptors set is by far the most effective in lowering \mathcal{K}_m , confirming that θ is a crucial part of the reaction coordinate³⁵.

Furthermore, the approximate linear relation between θ and φ in the TSE reported in ref. 35 is observed if and only if θ is included in the descriptors set. This point is illustrated in two top plots in Fig. 2c, where the margins of the $p_{\mathcal{K}}$ TSE distribution relative to φ and θ is drawn on the φ and θ free energy surface (see also Supplementary Fig. 12). In all cases, in this representation, the margins have an elongated ellipsoidal structure whose main axis is misaligned relative to the expected behavior if θ is not part, explicitly or implicitly, of the descriptor set. This shows that the combination φ , ψ , although efficient when used in an enhanced sampling context, does not fully capture the nature of the TSE. As a corollary to this analysis, we agree with ref. 35 that the alanine dipeptide free energy surface should be more expressively represented if drawn as a function of φ and θ as in Fig. 2 rather than using the standard φ , ψ projection since it brings out clearly the role of θ .

This instructive example also allows us to compare in practice our definition of the TSE based on $p_{\mathcal{K}}$ with the conventional one based on $q(\mathbf{x}) \approx \frac{1}{2}$. Indeed, the latter also includes unlikely configurations with extremely high energy, whereas our criterion focuses only on the physically relevant region (see also Supplementary Fig. 13).

In the alanine dipeptide case, we had enough prior knowledge of the system that we could solve the problem using a reduced set of descriptors. However, when one approaches a new system, this is rarely the case. For this reason, as a demonstration of the possibilities of our

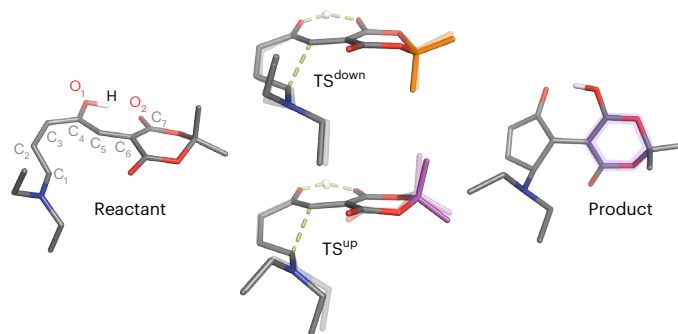


Fig. 3 | DASA reaction. Snapshots of reactant, product and transition species involved in DASA reaction in which carbon atoms are depicted in gray, oxygen in red, nitrogen in blue and the reactive hydrogen in white, whereas nonreactive hydrogens are omitted for clarity. On the reactant configuration, the labels highlight the atoms used to compute the distance-based descriptors set used for the training of the committor model, whereas the purple shadow on the product highlights the 1,3-dioxane ring used to compute the puckering coordinates. For the transition state (TS), we report two configurations that are representative of the TSE according to clustering and puckering analysis. In solid color, we report the medoids of each cluster, and in transparency, the corresponding reference configuration obtained via the dimer method⁶⁴. The atoms that characterize the TS^{down} configuration are highlighted in orange, whereas the TS^{up} ones are in purple. For such configurations, the bonds that change through the reaction are shown as dashed green lines.

method, we also take a blind approach and assume that we only know the initial and final conformations. For this physics-agnostic calculation, we use as descriptors the 45 distances between the alanine heavy atoms. At convergence, we find that this descriptor set does much better than the ones based on dihedrals only, reaching the value of $\mathcal{K}_m = 1.1$ a.u., where a.u. stands for arbitrary units, and the TS linear θ - φ correlation is respected, as shown at the bottom of Fig. 2c, since the θ degree of freedom is taken into account, albeit implicitly. This is not surprising, given the much higher variational flexibility of the trial committor function.

However, in so doing, we lose physical transparency, and the price for this unbiased generality is that further analysis is needed³⁶. To this effect, we use a tool exploited in ref. 33 that allows ranking the descriptors according to their weight in the optimized $q_{\theta}(\mathbf{x})$ model (see ‘Ranking of descriptors with feature relevance analysis’ section in Methods). From this ranking (Supplementary Fig. 10), it emerges that the two distances d_{α} and d_{β} (Fig. 2a) stand out as the most relevant. This might seem at first surprising, but we note that these two distances reflect the position of O relative to the plane that passes through N, C and C_{β} . In turn, the position of O depends on θ and φ ; thus, the prominence of d_{α} and d_{β} is a way in which the NN expresses the TSE conformation using only interatomic distances. Of course, the dihedrals are the natural language in which to describe a conformational change, while the description in terms of interatomic distances is less immediately evident, but it is reassuring that the physical conclusions are the same even if cast in a different language.

The results of this analysis guided us to take a fresh look at this much-studied problem. In fact, we noticed that a different way of expressing the alanine conformation can be obtained using as a descriptor the projection of the O coordinate on the direction perpendicular to the NCC_{β} plane (Supplementary Section 3C). It turns out that this single descriptor approximates the reaction coordinate extremely well, reaching a very low variational minimum at $\mathcal{K}_m = 1.2$ a.u., which is comparable, within the statistical uncertainty, with the one obtained using the full interatomic distance set as descriptors. This exercise illustrates clearly one of the advantages of our approach, namely the ability of the method to focus the researcher’s attention on where the real action is and to help design new efficient CVs.

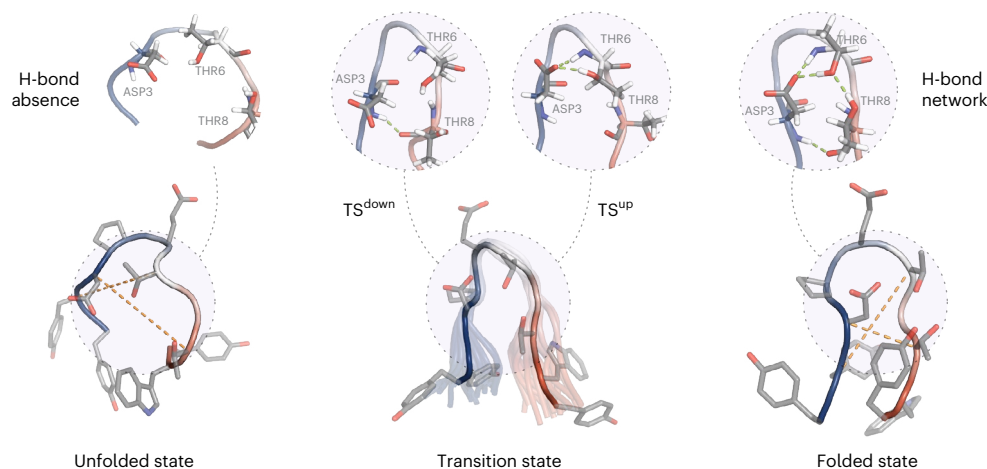


Fig. 4 | Chignolin folding. Snapshots of representative configurations from the folded (F), unfolded (U) and transition (TS) states (bottom row) of chignolin protein and the zoomed-in views, highlighted by the shaded circles, of the corresponding hydrogen bonds (top row). Carbon atoms are depicted in gray, oxygen in red, nitrogen in blue and hydrogen in white. In the bottom row, the main chain of the protein is depicted as a cartoon colored from blue to red according to the residue number from 1 to 10, whereas the side chains are

reported in transparency in licorice, and hydrogen atoms are omitted for clarity. For the F and U metastable states, we report as dashed orange lines the distances $C_2^2-C_6^6$ and $C_3^3-C_8^8$, which were found to be most important in our model. For the TS, we report in transparency the superimposition of 20 configurations from the TSE. In the top row, we highlight the crucial hydrogen bonds between the Asp3, Thr6 and Thr8 residues, and for the TS, we report the structures related to the medoids of the two clusters.

DASA reaction

Our third test is the 4π -electrocyclization of the donor–acceptor Stenhouse adduct (DASA), depicted in Fig. 3, that is part of a complex photo-switching pathway^{37–39}. This reaction involves a major conformational change, the formation of a cyclopentenone ring, and a proton transfer from O_1 to O_2 (ref. 40). The energy barrier associated with such transition is much larger than $k_B T$ (~ 1 eV (ref. 39)); thus, we expect the committor to have a very sharp step-like behavior. Although, in this case, it would probably have been more efficient to use standard methods based on the search for the stationary points of the potential energy surface, we found both instructive and challenging to solve the problem using our approach. Indeed, the iterative process needed to be adapted to the sharp features of the committor, as described in Methods.

As we are dealing with a chemical reaction involving the formation and breaking of bonds, it is natural to take the distances between atoms involved in such bond modifications as descriptors. In particular, we select as input features the distances between atoms labeled in Fig. 3 for a total of 45 input descriptors.

After having obtained the committor, we find that four distances are ranked higher than the others (Supplementary Fig. 15), which are, in order, the C_1-C_5 , C_1-O_1 , C_1-C_6 and C_2-O_2 distances. There are clear chemical reasons for this result. The formation of the C_1C_5 bond reflects the closure of the cyclopentenone ring, the three distances C_1-O_1 , C_1-C_6 and C_2-O_2 describe the conformational change that the molecule undergoes during the reaction and are operative in reducing the O_1-O_2 distance, thus allowing the proton to be transferred from O_1 to O_2 (Supplementary Fig. 18). Finally, the role of the C_1-C_6 distance in the reaction reflects the change in bonding length due to the C_5 hybridization change from sp^2 to sp^3 that takes place when the pentagonal ring closes.

Contrary to the case of the Müller potential and of alanine dipeptide, already from a visual inspection, it is clear that the TSE exhibits some complexity (Supplementary Fig. 17). Thus, we apply the k -medoids analysis³⁴ and find that the TSE can be described as composed of two classes, which can be distinguished by the different puckering⁴¹ of the 1,3-dioxane hexagonal ring, as shown in Fig. 3. If optimized, the two structures differ in energy by only $-1k_B T$; thus, they both are likely to be part of the TSE. This example, and more so the one

that follows, demonstrates the need to introduce the TSE concept, thus extending the more traditional view of associating a single configuration to the transition state.

Chignolin

The final test of our method is the study of the chignolin protein in solution, which is able to fold in a stable hairpin structure. Luckily, the unbiased 106- μ s-long trajectory performed by the D. E. Shaw group using a special purpose machine⁴² is available and provides a precious benchmark for our calculations.

In this case, we use as descriptors all the 45 distances that connect the 10 α -carbons as done in ref. 43. After reaching convergence of our procedure, by analyzing the 40-ns-long simulations of final iteration, we collected a large number of TSE configurations that, on visual inspection, appear to be very close to those obtained in the much longer unbiased dynamics of ref. 42. In fact, we find that, in all TSE configurations, the hairpin bend ($C_4^4-C_7^7$) is formed, and the two prongs of the hairpin are roughly aligned. However, the two protein segments ($C_1^1-C_4^4$) and ($C_7^7-C_{10}^{10}$) exhibit a variety of conformational arrangements, as depicted in Fig. 4. Luckily, the large number of TSE configurations we were able to collect allowed a statistically meaningful analysis of the TSE to be carried out and the apparent disorder to be understood.

As in the previous cases, we perform a relevance analysis of the descriptors in the optimized $q_\theta(\mathbf{x})$ as in ref. 33. We find two surprising results: none of the descriptors that can be associated with the formation of the hairpin bend plays a remarkable role. Instead, the two apparently improbable distances $C_2^2-C_6^6$ and $C_3^3-C_8^8$ emerge as rather relevant (Supplementary Fig. 19). In a first instance, this result can be understood if we notice that the hairpin bend is easily formed, and many unfolded structures share this feature (Supplementary Fig. 20). Furthermore, the role of the two distances can be attributed to the need to align the two prongs before folding, this being an important and entropy-costly step on the way to folding. But there is more to it, as we discovered by clustering the TSE data using again the k -medoids method³⁴. In fact, we find that the TSE configurations can be classified into two groups. In one, a bidentate H-bond is established between Asp3 and Thr6 (TSE^{up}). In the other, a monodentate H-bond links Asp3 and Thr8 (TSE^{down}) (see also Supplementary Fig. 21). We note that in the

folded state, both H-bonds are simultaneously formed, while in the unfolded state, the probability of finding either of these two bonds formed is very low (Supplementary Fig. 21).

Since the formation of these H-bonds was not explicitly included in the descriptors, the two distances $C_{\alpha}^2 - C_{\alpha}^6$ and $C_{\alpha}^3 - C_{\alpha}^8$ also act as proxies for the formation on the way to the folded state of either one of these two crucial H-bonds⁴⁴.

Discussion

In this paper, we have developed a strategy for tackling the rare event problem. This strategy is guided by Kolmogorov's variational principle for the determination of the committor function and has led us to define what we call the Kolmogorov ensemble, in which a committor-dependent bias is added to the interatomic potential. This is a rigorous extension of the notion of transition state and is indispensable to describe complex systems, like chignolin, DASA and many others⁴⁵, where it is not possible to identify a single configuration as the one through which the reaction has to pass. In complex cases, additional complications may also arise from the presence of unknown intermediate states that, once discovered, may either require splitting the problem into parts or longer convergence times. Another current limitation of our method is related to the use of physical descriptors as input, as their choice can be non-trivial in complex cases. In this regard, different architectures, for example, graph NNs, should be tested in the near future to directly operate on the atomic coordinates.

We have also shown that the variational principle provides a powerful tool for analyzing the TSE, identifying the most relevant degrees of freedom involved in the reaction and ranking them in a quantitative way. This and the availability of a large number of TSE configurations can help construct efficient CVs⁴³ for both enhancing sampling and summarizing the physics of the process under study. Knowledge of the TSE will also be extremely useful when building reactive machine learning potentials, where collecting data on the transition state has proven to be essential for obtaining reliable results⁴⁶.

However, the most promising perspective is that, from the sampling of the TSE, we could compare in the future with experimental observation coming, for instance, from time-resolved spectroscopy, and with the help of the analysis tools that we have developed, we can gain deep insight into reactive processes so as to be able to unveil enzymatic reaction mechanisms, steer a chemical reaction toward a desired product, design new drugs and even guide crystallization processes.

Methods

Self-consistent iterative procedure

As anticipated in the introduction, we represent the committor function $q(\mathbf{x})$ as the output of a NN $q_{\theta}(\mathbf{d}(\mathbf{x}))$, with θ trainable parameters, which takes as input a set of (physical) descriptors $\mathbf{d}(\mathbf{x})$ that are functions of the atomic coordinates \mathbf{x} . We optimize our model using the variational principle of equation (1). To do so, we use statistical sampling to evaluate the integral in $\mathcal{K}[q(\mathbf{x})]$ and rely on a self-consistent iterative procedure in which we alternate cycles of training to cycles of sampling. This section briefly presents only a schematic overview of the steps involved in such a procedure, discussing the details of the different components in the following sections.

- Step 1: The committor $q_{\theta}^n(\mathbf{x})$ at iteration n is constructed using the dataset of configurations \mathbf{x}^n and weights w_i^n updated from the previous iterations (see 'Optimization strategy' section). For the first iteration $n = 0$, we shall use a dataset consisting of configurations collected with unbiased simulations in the two metastable basins and labeled accordingly.
- Step 2: We perform biased simulations to sample the Kolmogorov ensemble defined in equation (3). These simulations can be started from the two basins or even from the TSE. We do this by applying the bias $V_{\mathcal{K}}^n(\mathbf{x}) = -\frac{1}{\beta} \log(|\nabla q_{\theta}^n(\mathbf{x})|^2)$ (see 'Sampling the

Kolmogorov ensemble' section). We check whether convergence has been reached. If not, we proceed to step 3.

- Step 3: We update our training set with the new sampled configurations, reweighing them by the applied bias $w_i^n = \frac{e^{\beta V_{\mathcal{K}}^n(\mathbf{x}_i)}}{\langle e^{\beta V_{\mathcal{K}}^n(\mathbf{x})} \rangle_{\mathcal{U}_{\mathcal{K}}^n}}$ (see 'Sampling the Kolmogorov ensemble' section) and repeat from step 1.

Optimization strategy

To optimize the committor model, we translate the Kolmogorov variational functional and the related boundary conditions into a loss function composed of two terms.

A key variational loss term L_v that is used to evaluate the functional in equation (1), as

$$L_v = \frac{1}{N^n} \sum_i w_i |\nabla_{\mathbf{u}} q(\mathbf{x}_i)|^2, \quad (5)$$

where we use as training set all the N^n configurations \mathbf{x}_i collected until iteration n together with their associated statistical weights w_i and $\nabla_{\mathbf{u}}$ denotes the gradient with respect to the mass-weighted coordinates $\mathbf{u}_i^j = \sqrt{m^j} \mathbf{x}_i^j$, in which m^j is the mass of atoms of type j .

This term is complemented by the boundary loss term L_b , which imposes the correct boundary conditions, that is, $q(\mathbf{x}_A) = 0$ and $q(\mathbf{x}_B) = 1$, and is expressed as

$$L_b = \frac{1}{N_A} \sum_{i \in A} (q(\mathbf{x}_i))^2 + \frac{1}{N_B} \sum_{i \in B} (q(\mathbf{x}_i) - 1)^2. \quad (6)$$

This term is computed only on the labeled dataset introduced in the first iteration $n = 0$ that consists of N_A unbiased configurations from state A and N_B configurations from state B.

The total loss function is thus obtained as a linear combination of these components

$$L = L_v + \alpha L_b, \quad (7)$$

in which we introduce the α hyperparameter to scale the relative contributions of the two terms during the optimization procedure. It is worth noting that, in the first iteration, the L_v contribution to the total loss will be minimal, as the dataset is limited to close-to-equilibrium configurations from the bottom of metastable states. Nonetheless, the L_b term still allows obtaining a reasonable first guess $q_{\theta}^0(\mathbf{x})$, which can be seen as a classifier trained to distinguish between states A and B. This is not surprising considering that a very similar approach has often been used to design machine learning CVs for enhanced sampling^{33,47}.

Sampling the Kolmogorov ensemble

As discussed in the introduction, the variational approach of equation (1) and the corresponding loss term of equation (5) are of little use if the TSE, where $|\nabla q(\mathbf{x})|^2$ is substantially different from zero, is poorly represented in the training dataset.

In previous applications of the Kolmogorov variational principle, enhanced sampling methods were used to collect data in the TS region^{23,28}. However, they relied on the use of CVs, and even assuming that the CV is able to capture the TSE main features, they had to spend time sampling over and over uninteresting regions of the configuration space, such as those belonging to the metastable states.

In contrast, we apply to the system a bias that is attractive in the TS region and repulsive in the basin regions. Even using a simplified model for $q_{\theta}(\mathbf{x})$ the addition of the potential

$$V_{\mathcal{K}}(\mathbf{x}) = -\frac{1}{\beta} \log(|\nabla q_{\theta}(\mathbf{x})|^2 + \epsilon), \quad (8)$$

where ϵ is a positive regularization term, biases the sampling toward the TS and away from basins A and B. Thus, already after the first iterations, TSE configurations are being harvested and attention is taken away from the metastable basins. It should be noted that, in practice, the bias in equation (8) can be computed by the gradient with respect to the input features of q_θ for a simpler and faster interface with PLUMED⁴⁸ (see ‘Codes and software’ section). At convergence, the results will not depend on this choice since, when computing $\mathcal{K}[q(\mathbf{x})]$, the configurations thus generated are reweighed to give them the correct Boltzmann weight. This is done by associating each configuration i that was added to the training set at iteration n with a weight

$$w_i^n = \frac{e^{\beta V_{\mathcal{K}}^n(\mathbf{x}_i)}}{\langle e^{\beta V_{\mathcal{K}}^n(\mathbf{x})} \rangle_{U_{\mathcal{K}}^n}} \quad (9)$$

that does not explode exponentially given the logarithmic nature of the bias equation (8).

Tips and tricks for optimization

In our experience, the straightforward version of the iterative method presented above leads to convergence after an affordable number of iterations. However, to accelerate convergence, it is expedient to introduce some modification to the self-consistent cycle guided, if possible, by previous qualitative knowledge of the system.

For example, as the configurations from the first iteration labeled dataset are unbiased, they are assigned unitary weights $w_{i \in A}^0 = w_{i \in B}^0 = \exp(\beta V_{\mathcal{K}}^0(\mathbf{x}_i)) = 1$. This implicitly implies that, in the Boltzmann ensemble, the two metastable states have the same energy and can be sampled with the same probability. In spite of this unphysical assumption, after a few iterations, the correct relative statistical weight between the points in the two basins is re-established. However, the number of iterations needed to reach convergence can be reduced if we have an even approximate estimate of the free energy difference ΔF_{AB} between the initial and final basin. In such a case, we can use a less approximate dataset on which we modify the weights of the initial points in B as

$$w_{i \in B}^0 = 1 \rightarrow \tilde{w}_{i \in B} = \exp(-\beta \Delta F_{AB}) \quad (10)$$

to make the underlying distribution resemble more closely the Boltzmann one (Supplementary Fig. 9).

Of course, if we have other information on the TSE coming, for instance, from enhanced sampling simulations or successful molecular dynamics runs in which reactive trajectories have been obtained, we can use them from the initial iteration to obtain a better starting guess and a speedier convergence.

Since the bias is used here to speed up the calculation, we are at liberty to change its magnitude, provided that the data collected are properly reweighed. In this respect, the simplest and most controllable device is to multiply the bias in equation (8) by a positive multiplicative factor λ ,

$$V_K(\mathbf{x}) \rightarrow \tilde{V}_K(\mathbf{x}) = \lambda V_K(\mathbf{x}). \quad (11)$$

In the first iteration, we run several parallel simulations with different values $\lambda \approx 1$, choose among the λ values tested the smallest that is capable of attracting the system to the TSE, and in the following iterations, we keep λ fixed to this value. In the case of DASA, which is representative of systems in which the committor changes very quickly in a small region of configuration space such that $|\nabla q(\mathbf{x})|^2$ can assume large values, the bias can become too large and trap the system in the TSE. To remedy this problem, from the second iteration, we explore the effect of a range of $\lambda \approx 1$ values and this time, we choose the largest value of λ that allows escaping the TSE and we maintain this value in the following iteration. In hard cases, one can further optimize the value of λ

at each iteration, varying λ in a small range of values and picking again the one that is most effective. It must be added that the computer time invested in the simulations needed to improve the choice of λ is not wasted, as the configurations and statistical weights thus collected can be added to the training set and thus used to improve our estimation of the integral in $\mathcal{K}[q(\mathbf{x})]$.

To avoid an artificial bias, the data needed to pass at successive iterations are collected by combining data from simulations that start from both A and B. However, if, as in the case of the DASA, $|\nabla q(\mathbf{x})|^2$ is strongly peaked, once the TSE has been visited, it is helpful to start the successive iterations also from TSE configurations. This is because, when the committor has a sharp step-like behavior, the action of the bias will be confined to a very narrow region, eventually making it difficult for simulations that start from either A or B to reach the TSE region.

Based on the variational nature of the optimization criterion, the \mathcal{K}_m value, as estimated in practice in equation (5), typically suffices as a figure of merit for monitoring the convergence of the procedure and the accuracy of the obtained model. However, if desired, further evaluation could be performed by training a committee of models to obtain a statistical measure of the model uncertainty, similarly to what is commonly done when dealing with machine learning potentials⁴⁶.

Motivation of variational principle

The committor function $q(\mathbf{x})$ for the transition process from a state A to a state B, under the hypothesis of overdamped dynamics, can be obtained as the solution of a set of partial differential equations²⁰

$$\begin{cases} \nabla U(\mathbf{x}) \cdot \nabla q(\mathbf{x}) - \beta^{-1} \Delta q(\mathbf{x}) = 0 & \mathbf{x} \notin (A \cup B) \\ q(\mathbf{x}) = 0 & \mathbf{x} \in A \\ q(\mathbf{x}) = 1 & \mathbf{x} \in B \end{cases}, \quad (12)$$

where $U(\mathbf{x})$ is the interatomic potential. Unfortunately, this can only be solved for extremely simple toy models, such as the toy double well potential reported in Supplementary Fig. 2. However, an equivalent solution can also be obtained by minimization of the variational functional $\mathcal{K}[q(\mathbf{x})]$ (ref. 20) under the same boundary conditions

$$\mathcal{K}[q(\mathbf{x})] = \frac{1}{\mathcal{Z}} \int |\nabla q(\mathbf{x})|^2 e^{-\beta U(\mathbf{x})} d\mathbf{x} \quad \mathbf{x} \notin (A \cup B), \quad (13)$$

where $\mathcal{Z} = \int e^{-\beta U(\mathbf{x})} d\mathbf{x}$ is the partition function corresponding to $U(\mathbf{x})$.

We then observe that the variational functional of equation (13) can also be written as the ensemble average of the $|\nabla q(\mathbf{x})|^2$ quantity over the Boltzmann ensemble driven by the potential $U(\mathbf{x})$, as reported in equation (1) in the introduction.

$$\mathcal{K}[q(\mathbf{x})] = \frac{\int |\nabla q(\mathbf{x})|^2 e^{-\beta U(\mathbf{x})} d\mathbf{x}}{\mathcal{Z}} = \langle |\nabla q(\mathbf{x})|^2 \rangle_{U(\mathbf{x})}. \quad (14)$$

Despite being derived under the overdamped dynamics hypothesis, this whole formalism can also be extended to the general case of Langevin equation by introducing a few reasonable approximations that do not affect the final results, as discussed in detail in ref. 20.

Ranking of descriptors with feature relevance analysis

To identify the most relevant inputs in our learned committor models, we rank the input descriptors by performing a feature relevance analysis. This is based on the derivatives of the committor model $q_\theta(d(\mathbf{x}))$ with respect to the descriptors $d(\mathbf{x})$, and the rank r^k of descriptor k is defined as

$$r^k = \sum_{x_i \in \text{TSE}} \left| \frac{\partial q}{\partial d^k} \right| \sigma(d^k), \quad (15)$$

where the sum is performed over a subset of the sampled TSE configurations, filtered for simplicity to have $0.4 < q < 0.6$, and $\sigma(d^k)$ is the standard deviation of descriptor d^k over this set. We must note, however, that different approaches to feature relevance analysis in NNs are available in specific machine learning literature^{36,49}.

Choice of NN activation functions

Considering that, in our approach, the derivatives of the output of the NN model are as important as the output itself, we used as an activation function for the hidden layers the hyperbolic tangent function (tanh). This indeed provides a good trade-off between nonlinear contribution to the model and guaranteeing stable and smooth derivatives²⁷.

Moreover, to facilitate the learning of a $q_\theta(\mathbf{x})$ with the correct shape, we used a sharp sigmoid-like activation $s(y)$ for the last layer

$$s(y) = \frac{1}{1 + e^{-3y}}. \quad (16)$$

Codes and software

The reported NN-based committor models are based on the Python machine learning library PyTorch⁵⁰. The specific code for the definition and the training of the model is developed in the framework of the open-source mlcolvar⁵¹ library. The committor-based enhanced sampling simulations have been performed using the open-source plugin PLUMED⁵² 2.9, modifying the PYTORCH_MODEL interface available in the optional pytorch⁵¹ module of the code. This has been patched with different molecular dynamics (MD) engines to simulate the reported systems. The Müller–Brown potential's simulations have been performed using the MD engine in the ves_md_linearexpansion⁵³ module of PLUMED. The vacuum alanine dipeptide simulations have been carried out using the GROMACS v2021.5⁵⁴ MD engine and the Amber99-SB⁵⁵ force field. The DASA reaction simulations have been carried out using the CP2K-8.1⁵⁶ software package at the PM6 semi-empirical level⁵⁷. For the study of folding and unfolding of chignolin in explicit solvent, we performed our simulations using GROMACS v2021.5⁵⁴ the CHARMM22⁵⁸ force field and TIP3P⁵⁹ water force field. All the reported molecular snapshots have been produced using the open-source PyMOL⁶⁰ code, whereas the clustering analyses have been performed using the k -medoids method as implemented in the kmedoids³⁴ Python library.

Data availability

Training and simulation data and inputs are available on [GitHub](#) ref. 61 and on [Zenodo](#) ref. 62. PLUMED input files are also available on the PLUMED-NEST⁴⁸ repository with [plumID:24.011](#) ref. 63. Source data are provided with this paper.

Code availability

The code for the definition and training of NN-based committor model is available through the open-source mlcolvar library⁵¹, which is the preferred way to access the code. Nonetheless, a frozen version of the library is available on [Zenodo](#) ref. 62. The PLUMED bias interface is available on [GitHub](#) ref. 61, on [Zenodo](#) ref. 62 and on the PLUMED-NEST⁴⁸ repository with [plumID:24.011](#) ref. 63.

References

- Solomons, T. G. & Fryhle, C. B. *Organic Chemistry* (Wiley, 2008).
- Anslyn, E. V. & Dougherty, D. A. *Modern Physical Organic Chemistry* (University Science Books, 2006).
- Baldwin, R. L. & Rose, G. D. Is protein folding hierarchic? II. Folding intermediates and transition states. *Trends Biochem. Sci.* **24**, 77–83 (1999).
- Cecconi, C., Shank, E. A., Bustamante, C. & Marqusee, S. Direct observation of the three-state folding of a single protein molecule. *Science* **309**, 2057–2060 (2005).
- Jackson, S. E. How do small single-domain proteins fold? *Fold. Des.* **3**, R81–R91 (1998).
- Torrie, G. M. & Valleau, J. P. Nonphysical sampling distributions in Monte Carlo free-energy estimation: umbrella sampling. *J. Comput. Phys.* **23**, 187–199 (1977).
- Laio, A. & Parrinello, M. Escaping free-energy minima. *Proc. Natl Acad. Sci. USA* **99**, 12562–12566 (2002).
- Izrailev, S. et al. Steered molecular dynamics. In *Computational Molecular Dynamics: Challenges, Methods, Ideas. Lecture Notes in Computational Science and Engineering*, vol. 4. (eds Deuffhard, P. et al.) https://doi.org/10.1007/978-3-642-58360-5_2 (Springer, 1999).
- Darve, E. & Pohorille, A. Calculating free energies using average force. *J. Chem. Phys.* **115**, 9169–9183 (2001).
- Sugita, Y. & Okamoto, Y. Replica-exchange molecular dynamics method for protein folding. *Chem. Phys. Lett.* **314**, 141–151 (1999).
- Hénin, J., Lelièvre, T., Shirts, M. R., Valsson, O. & Delemotte, L. Enhanced sampling methods for molecular dynamics simulations. *Living J. Comput. Mol. Sci.* **4**, 1583 (2022).
- Kolmogorov, A. Über die analytischen Methoden in der Wahrscheinlichkeitsrechnung. *Math. Ann.* **104**, 415–458 (1931).
- Onsager, L. Initial recombination of ions. *Phys. Rev.* **54**, 554–557 (1938).
- Berezhkovskii, A. & Szabo, A. One-dimensional reaction coordinates for diffusive activated rate processes in many dimensions. *J. Chem. Phys.* **122**, 014503 (2005).
- Berezhkovskii, A. M. & Szabo, A. Diffusion along the splitting/commitment probability reaction coordinate. *J. Phys. Chem. B* **117**, 13115–13119 (2013).
- Du, R., Pande, V. S., Grosberg, A. Y., Tanaka, T. & Shakhnovich, E. S. On the transition coordinate for protein folding. *J. Chem. Phys.* **108**, 334–350 (1998).
- W, E., Ren, W. & Vanden-Eijnden, E. Transition pathways in complex systems: reaction coordinates, isocommittor surfaces, and transition tubes. *Chem. Phys. Lett.* **413**, 242–247 (2005).
- Dellago, C., Bolhuis, P. & Geissler, P. In *Computer Simulations in Condensed Matter Systems: From Materials to Chemical Biology* Vol. 1 (eds Ferrario, M., Ciccotti, G. & Binder, K.) 349–391 (Springer, 2006).
- Vanden-Eijnden, E. Transition Path Theory. in *Computer Simulations in Condensed Matter Systems: From Materials to Chemical Biology Volume 1. Lecture Notes in Physics*, vol. 703 (eds Ferrario, M. et al.) https://doi.org/10.1007/3-540-35273-2_13 (Springer, 2006).
- W, E. & Vanden-Eijnden, E. Transition-path theory and path-finding algorithms for the study of rare events. *Annu. Rev. Phys. Chem.* **61**, 391–420 (2010).
- Roux, B. Transition rate theory, spectral analysis, and reactive paths. *J. Chem. Phys.* **156**, 134111 (2022).
- Jung, H. et al. Machine-guided path sampling to discover mechanisms of molecular self-organization. *Nat. Comput. Sci.* **3**, 334–345 (2023).
- Rotskoff, G. M., Mitchell, A. R. & Vanden-Eijnden, E. Active importance sampling for variational objectives dominated by rare events: consequences for optimization and generalization. In *Proc. 2nd Mathematical and Scientific Machine Learning Conference* Vol. 145 (eds Bruna, J., Hesthaven, J. & Zdeborova, L.) 757–780 (PMLR, 2022).
- Chen, H., Roux, B. & Chipot, C. Discovering reaction pathways, slow variables, and committor probabilities with machine learning. *J. Chem. Theory Comput.* **19**, 4414–4426 (2023).
- Bolhuis, P. G., Chandler, D., Dellago, C. & Geissler, P. L. Transition path sampling: throwing ropes over rough mountain passes, in the dark. *Annu. Rev. Phys. Chem.* **53**, 291–318 (2002).

26. Lazzeri, G., Jung, H., Bolhuis, P. G. & Covino, R. Molecular free energies, rates, and mechanisms from data-efficient path sampling simulations. *J. Chem. Theory Comput.* **19**, 9060–9076 (2023).
27. Khoo, Y., Lu, J. & Ying, L. Solving for high-dimensional committor functions using artificial neural networks. *Res. Math. Sci.* **6**, 1–13 (2019).
28. Li, Q., Lin, B. & Ren, W. Computing committor functions for the study of rare events using deep learning. *J. Chem. Phys.* **151**, 054112 (2019).
29. Chen, Y., Hoskins, J., Khoo, Y. & Lindsey, M. Committor functions via tensor networks. *J. Comput. Phys.* **472**, 111646 (2023).
30. Krivov, S. V. Nonparametric analysis of nonequilibrium simulations. *J. Chem. Theory Comput.* **17**, 5466–5481 (2021).
31. Krivov, S. V. Protein folding free energy landscape along the committor—the optimal folding coordinate. *J. Chem. Theory Comput.* **14**, 3418–3427 (2018).
32. Ma, A. & Dinner, A. R. Automatic method for identifying reaction coordinates in complex systems. *J. Phys. Chem. B* **109**, 6769–6779 (2005).
33. Bonati, L., Rizzi, V. & Parrinello, M. Data-driven collective variables for enhanced sampling. *J. Phys. Chem. Lett.* **11**, 2998–3004 (2020).
34. Schubert, E. & Lenssen, L. Fast k-medoids clustering in rust and Python. *J. Open Source Softw.* **7**, 4183 (2022).
35. Bolhuis, P. G., Dellago, C. & Chandler, D. Reaction coordinates of biomolecular isomerization. *Proc. Natl Acad. Sci. USA* **97**, 5877–5882 (2000).
36. Novelli, P., Bonati, L., Pontil, M. & Parrinello, M. Characterizing metastable states with the help of machine learning. *J. Chem. Theory Comput.* **18**, 5195–5202 (2022).
37. Zulfikri, H. et al. Taming the complexity of donor-acceptor Stenhouse adducts: infrared motion pictures of the complete switching pathway. *J. Am. Chem. Soc.* **141**, 7376–7384 (2019).
38. Stricker, F. et al. A multi-stage single photochrome system for controlled photoswitching responses. *Nat. Chem.* **14**, 942–948 (2022).
39. Raucci, U., Sanchez, D. M., Martínez, T. J. & Parrinello, M. Enhanced sampling aided design of molecular photoswitches. *J. Am. Chem. Soc.* **144**, 19265–19271 (2022).
40. Sanchez, D. M., Raucci, U. & Martínez, T. J. In silico discovery of multistep chemistry initiated by a conical intersection: the challenging case of donor-acceptor Stenhouse adducts. *J. Am. Chem. Soc.* **143**, 20015–20021 (2021).
41. Cremer, D. T. & Pople, J. General definition of ring puckering coordinates. *J. Am. Chem. Soc.* **97**, 1354–1358 (1975).
42. Lindorff-Larsen, K., Piana, S., Dror, R. O. & Shaw, D. E. How fast-folding proteins fold. *Science* **334**, 517–520 (2011).
43. Ray, D., Trizio, E. & Parrinello, M. Deep learning collective variables from transition path ensemble. *J. Chem. Phys.* **158**, 204102 (2023).
44. Bonati, L., Piccini, G. & Parrinello, M. Deep learning the slow modes for rare events sampling. *Proc. Natl Acad. Sci. USA* **118**, e2113533118 (2021).
45. Bonati, L. et al. The role of dynamics in heterogeneous catalysis: surface diffusivity and N₂ decomposition on Fe(111). *Proc. Natl Acad. Sci. USA* **120**, e2313023120 (2023).
46. Yang, M., Bonati, L., Polino, D. & Parrinello, M. Using metadynamics to build neural network potentials for reactive events: the case of urea decomposition in water. *Catal. Today* **387**, 143–149 (2022).
47. Trizio, E. & Parrinello, M. From enhanced sampling to reaction profiles. *J. Phys. Chem. Lett.* **12**, 8621–8626 (2021).
48. The Plumed consortium. Promoting transparency and reproducibility in enhanced molecular simulations. *Nat. Methods* **16**, 670–673 (2019).
49. Pizarroso, J., Portela, J. & Muñoz, A. Neursens: sensitivity analysis of neural networks. *J. Stat. Softw.* **102**, 1–36 (2022).
50. Paszke, A. et al. Pytorch: an imperative style, high-performance deep learning library. *Adv. Neural Inform. Process. Syst.* **32**, (2019).
51. Bonati, L., Trizio, E., Rizzi, A. & Parrinello, M. A unified framework for machine learning collective variables for enhanced sampling simulations: mlcolvar. *J. Chem. Phys.* **159**, 014801 (2023).
52. Tribello, G. A., Bonomi, M., Branduardi, D., Camilloni, C. & Bussi, G. PLUMED 2: new feathers for an old bird. *Comput. Phys. Commun.* **185**, 604–613 (2014).
53. Valsson, O. & Parrinello, M. Variational approach to enhanced sampling and free energy calculations. *Phys. Rev. Lett.* **113**, 090601 (2014).
54. Abraham, M. J. et al. Gromacs: high performance molecular simulations through multi-level parallelism from laptops to supercomputers. *SoftwareX* **1**, 19–25 (2015).
55. Salomon-Ferrer, R., Case, D. A. & Walker, R. C. An overview of the amber biomolecular simulation package. *WIREs Comput. Mol. Sci.* **3**, 198–210 (2013).
56. Kühne, T. D. et al. CP2K: An electronic structure and molecular dynamics software package—Quickstep: efficient and accurate electronic structure calculations. *J. Chem. Phys.* **152**, 194103 (2020).
57. Stewart, J. J. Optimization of parameters for semiempirical methods V: modification of nddo approximations and application to 70 elements. *J. Mol. Model.* **13**, 1173–1213 (2007).
58. Piana, S., Lindorff-Larsen, K. & Shaw, D. E. How robust are protein folding simulations with respect to force field parameterization? *Biophys. J.* **100**, L47–L49 (2011).
59. MacKerell, A. D. J. et al. All-atom empirical potential for molecular modeling and dynamics studies of proteins. *J. Phys. Chem. B* **102**, 3586–3616 (1998).
60. *The PyMOL Molecular Graphics System, Version 2.5* (Schrödinger, LLC, 2015).
61. Committor. GitHub <https://github.com/alphatestK/Committor> (2024).
62. Kang, P., Trizio, E. & Parrinello, M. Computing the committor with the committor: an anatomy of the transition state ensemble. *Zenodo* <https://doi.org/10.5281/zenodo.11164167> (2024).
63. PLUMED-NEST. <https://www.plumed-nest.org/eggs/24/011/> (PLUMED Consortium, 2024).
64. Henkelman, G. & Jónsson, H. A dimer method for finding saddle points on high dimensional potential surfaces using only first derivatives. *J. Chem. Phys.* **111**, 7010 (1999).

Acknowledgements

The authors acknowledge U. Raucci for the suggestions about the DASA, D. Ray for the hints on clustering methods, A. Rizzi and L. Bonati for code design contributions and F. Mambretti for the many helpful conversations and for carefully reading the manuscript.

Author contributions

All the authors equally contributed to the manuscript by conceptualizing the project, developing the theoretical methodologies and participating in the writing of the manuscript. Specifically, P.K. and E.T. developed the code for the training of the committor function and conducted the computational simulations.

Competing interests

The authors declare no competing interest.

Additional information

Supplementary information The online version contains supplementary material available at <https://doi.org/10.1038/s43588-024-00645-0>.

Correspondence and requests for materials should be addressed to Michele Parrinello.

Peer review information *Nature Computational Science* thanks Sergei V. Krivov, Omar Valsson and the other, anonymous, reviewer(s) for their contribution to the peer review of this work. Primary Handling Editor: Kaitlin McCardle, in collaboration with the *Nature Computational Science* team. Peer reviewer reports are available.

Reprints and permissions information is available at www.nature.com/reprints.

Publisher's note Springer Nature remains neutral with regard to jurisdictional claims in published maps and institutional affiliations.

Springer Nature or its licensor (e.g. a society or other partner) holds exclusive rights to this article under a publishing agreement with the author(s) or other rightsholder(s); author self-archiving of the accepted manuscript version of this article is solely governed by the terms of such publishing agreement and applicable law.

© The Author(s), under exclusive licence to Springer Nature America, Inc. 2024